

Accepted for publication in *Astrophys J.*

Dynamics and neutrino signal of black hole formation in non-rotating failed supernovae. I. EOS dependence

K. Sumiyoshi

Numazu College of Technology, Ooka 3600, Numazu, Shizuoka 410-8501, Japan

`sumi@numazu-ct.ac.jp`

S. Yamada

*Science and Engineering & Advanced Research Institute for Science and Engineering,
Waseda University, Okubo, 3-4-1, Shinjuku, Tokyo 169-8555, Japan*

and

H. Suzuki

*Faculty of Science and Technology, Tokyo University of Science,
Yamazaki 2641, Noda, Chiba 278-8510, Japan*

ABSTRACT

We study the black hole formation and the neutrino signal from the gravitational collapse of a non-rotating massive star of $40 M_{\odot}$. Adopting two different sets of realistic equation of state (EOS) of dense matter, we perform the numerical simulations of general relativistic ν -radiation hydrodynamics under the spherical symmetry. We make comparisons of the core bounce, the shock propagation, the evolution of nascent proto-neutron star and the resulting re-collapse to black hole to reveal the influence of EOS. We also explore the influence of EOS on the neutrino emission during the evolution toward the black hole formation. We find that the speed of contraction of the nascent proto-neutron star, whose mass increases fast due to the intense accretion, is different depending on the EOS and the resulting profiles of density and temperature differ significantly. The black hole formation occurs at 0.6–1.3 sec after bounce when the proto-neutron star exceeds its maximum mass, which is crucially determined by the EOS. We find that the average energies of neutrinos increase after bounce because of rapid temperature increase, but at different speeds depending on the

EOS. The duration of neutrino emission up to the black hole formation is found different according to the different timing of re-collapse. These characteristics of neutrino signatures are distinguishable from those for ordinary proto-neutron stars in successful core-collapse supernovae. We discuss that a future detection of neutrinos from black-hole-forming collapse will contribute to reveal the black hole formation and to constrain the EOS at high density and temperature.

Subject headings: supernovae: general — stars: neutron — black hole physics — neutrinos — hydrodynamics — equation of state

1. Introduction

Massive stars having more than ~ 10 solar masses (M_{\odot}) end their lives when the iron core is formed after the stages of nuclear burning (Bethe 1990). For the massive stars of ~ 10 – $20M_{\odot}$, the spectacular events known as supernova explosions occur due to the gravitational collapse of iron core and the launch of shock wave by the bounce of core at high density. A successful explosion leaves a proto-neutron star which emits a bunch of neutrinos during the formation and cools down (Burrows 1988; Suzuki 1994). This duration, (~ 20 s), of supernova neutrinos is determined by the time scale of diffusion of neutrinos in dense matter inside the proto-neutron star. In the case of SN 1987A, the burst of neutrinos was detected at the terrestrial detectors (Bionta et al. 1987; Hirata et al. 1987) and has proved the general scenario of supernova explosion and the formation of dense compact object (Sato & Suzuki 1987).

Stars more massive than $\sim 20M_{\odot}$ may have different fates. They usually have larger iron cores and will be intrinsically too massive to have stellar explosion. Then, the outcome will be a formation of black hole regardless of detailed scenarios. Although the number of such black-hole-forming massive stars is uncertain depending on the mass range and the initial mass function, it definitely consists of a portion of the stellar mass distribution and can be a substantial fraction. Therefore, it is important to clarify the general feature of black-hole-forming phenomena in a broader context of the gravitational collapse of massive stars. It is especially exciting to predict the neutrino signals from this type of events as a clear and unique identification of the black hole formation. The calculated template of neutrino signal will be decisive to identify the black hole formation in the Galaxy, if occurs, by the terrestrial neutrino research facilities.

Astronomically, the fate of massive stars beyond the mass limit ($\sim 20M_{\odot}$) for ordinary supernovae is currently attracting interest (Heger et al. 2003). Recent analyses of the ob-

served light curves of supernovae with the explosive nucleosynthesis suggest that there are novel categories of explosive phenomena with kinetic energies and ejected ^{56}Ni mass being different from those for the ordinary supernovae (Maeda & Nomoto 2003). In fact, faint supernovae and hypernovae might be the outcomes of massive stars in the range of $\sim 20\text{--}60M_{\odot}$. They differ from each other probably in the degree of rotation and fall-back, and are supposed to form a black hole regardless and are clearly distinguished from the ordinary supernovae forming neutron stars. Gamma ray bursts are thought to be commonly associated with the hypernovae (collapsars) (MacFadyen & Woosley 1999). The survey of the fate as a function of mass and metallicity is important to understand the evolution of galaxies and the Universe.

The scenarios for the formation of stellar mass black hole have been argued in several different contexts and the associated neutrino bursts have been studied in some cases. In the case of successful explosions from the massive stars of $\sim 10\text{--}20M_{\odot}$, some of the proto-neutron stars after the birth may evolve toward the black hole even after the launch of shock wave.

In most of supernova explosions, the accretion of material ceases within several 100 msec after bounce and a proto-neutron star is born with a fixed total baryon mass. Since the maximum mass of proto-neutron stars, which are hot and lepton-rich, can be larger than the maximum mass of cold neutron stars, massive proto-neutron stars in a certain mass range can lead to the black hole formation during the cooling and deleptonization (Glendenning 1995). The scenario of metastable proto-neutron stars relies on the equation of state of dense matter having the appearance of exotica such as hyperons, kaon condensates and quarks during the cooling through neutrino emissions (Keil & Janka 1995; Pons et al. 1999, 2001a,b). The emergence of neutrinos diffusing out from proto-neutron stars has been calculated in the flux-limited diffusion approximation during the quasi-hydrostatic evolution (Pons et al. 1999). In the case of metastable proto-neutron stars, the termination of neutrino burst is predicted to occur in 1 sec – 100 sec, which largely depends on the internal composition. The disappearance occurs during the exponential decrease of neutrino luminosities, which is common in the long-term proto-neutron star cooling. The delayed collapse of a proto-neutron star in this context has been studied in the dynamical simulations with general relativistic treatment to follow the final moment of black hole formation and the associated neutrino signals by the leakage or diffusion scheme (Baumgarte et al. 1996a,b).

The collapse to the black hole can be triggered if there is a significant fall back of material after the successful supernova explosion. The fall back in supernovae is used as a given ingredient in the studies of explosive nucleosynthesis, but has not been well established in the context of explosion mechanism. The amount and time scale of fall back is uncertain especially in the numerical simulations of supernova explosion, whose puzzle has not been

solved yet. In the aim of examining the supernova neutrinos from SN1987A, the quasi-static evolutions of proto-neutron star leading in some cases to the black hole formation have been studied for the assumed accretion rate (Burrows 1988). The numerical simulations have been done by solving the quasi-static evolution with the flux-limited diffusion approximation, therefore, the general relativistic instability was assumed to occur when the numerical code can not find a static solution. The characteristics of neutrino signals in the case of black hole formation were pointed out with the uncertainties in accretion rate and equation of state.

The current study focuses on the black hole formation without supernova explosion from massive stars of $\gtrsim 20M_{\odot}$, being different from the delayed collapse of proto-neutron star in successful explosions discussed above. Having large iron cores, the shock wave can not propagate outward and the standing accretion shock is settled above the proto-neutron star. The material of outer layers falls down continuously from the beginning of gravitational collapse. The mass of proto-neutron star increases accordingly toward the maximum mass and the dynamical collapse to the black hole takes place. There is no bright optical display associated with the collapse accordingly.

We aim to clarify the sequence of evolution starting from the beginning of gravitational collapse of a massive star of $40M_{\odot}$ to the final moment of black hole formation. In order to predict the time profile of neutrino burst and the energy spectrum of neutrinos as well as the dynamical evolution, we perform elaborate simulations of ν -radiation hydrodynamics in general relativity. We follow the evolution of proto-neutron star with matter accretion for a long time (~ 1 s), which is challenging numerically with the exact treatment of ν -radiation hydrodynamics, to find when and how the black hole is formed.

The explosion energies and their dependence on progenitor models have been studied by two-dimensional simulations of hydrodynamics with a simplified neutrino treatment for 15, 25 and $40M_{\odot}$ stars (Fryer 1999). Although the border line for black hole formation without explosion has been estimated to be roughly $40M_{\odot}$, the simplified treatment of neutrinos has allowed the author to provide only an approximate limit for success of explosion and the evolution of proto-neutron star toward black hole has not been studied in his simulations. A simulation of general relativistic ν -radiation hydrodynamics has been first done by Liebendoerfer et al. (2004) and the numerical result for a $40M_{\odot}$ star leading to the black hole formation has been reported with the detailed description of numerical code and test bed for core-collapse supernovae but for a single EOS.

Rapid formations of black hole after the birth of proto-neutron star can be crucially affected by the equation of state (EOS) of dense matter. The maximum mass of evolving proto-neutron stars is determined by the stiffness of EOS and the degree of deleptonization. In addition, the initial profile of proto-neutron star is determined right after the core bounce,

which is influenced by the EOS also. Recently, different EOS's for supernova simulations have become available (Lattimer & Swesty 1991; Shen et al. 1998) and the detailed comparisons of core collapse from a $15M_{\odot}$ star, which is supposed to explode forming a neutron star, have been made in the ν -radiation hydrodynamics (Sumiyoshi et al. 2005). It has become apparent that the profiles of proto-neutron star long after bounce are significantly different depending on the EOS and the resulting spectra of neutrinos are distinct. Therefore, it is essential to examine the influence of the EOS on the evolution toward the black hole formation and to predict the associated neutrino signals. We note again that the single EOS (Lattimer & Swesty 1991) has been adopted in the previous study by Liebendoerfer et al. (2004) and the crucial influence of EOS has not been explored yet.

In the current study, we make the first comparison of the dynamical formations of black hole from a massive star with ν -radiation hydrodynamics by adopting two sets of EOS. We aim to clarify the difference of dynamical evolutions due to the EOS's in order to probe the dense matter. In the black-hole-forming collapse, the central core experiences higher densities and temperatures than in normal supernovae as we will show. It is especially interesting to reveal the differences in neutrino signals in order to extract the information of EOS from terrestrial neutrino detections in future. We will argue that the duration of neutrino burst from the black-hole-forming collapse can put a constraint on the stiffness of EOS and the phase transition point to exotic phases (Sumiyoshi et al. 2006).

We arrange this article as follows. We begin with the descriptions on the numerical simulations in § 2, including the numerical code, the physical inputs, the initial setting and the criterion for black hole formation. We report in order the numerical simulations in § 3, describing the evolution of core-collapse, proto-neutron star evolution and the second collapse to black hole. The evolution of neutrino distributions and EOS-dependences in neutrino signals are presented in § 3.5 and 3.6, respectively. Implications of current results for the EOS study are discussed in § 4. We end up with a summary in § 5.

2. Numerical Simulations

2.1. Numerical Code

We adopt the numerical code of general relativistic ν -radiation hydrodynamics that solves the Boltzmann equation for neutrinos together with lagrangian hydrodynamics under the spherical symmetry (Yamada 1997; Yamada et al. 1999; Sumiyoshi et al. 2005). The numerical code has been successfully applied to study the core collapse in the case of a $15M_{\odot}$ star as the progenitor (Sumiyoshi et al. 2005). It is a fully implicit code in order to

follow the long-term evolution of supernova core for more than 1 s after bounce and has a rezoning feature to efficiently capture the accretion of outer layer onto the compact object. The same numerical treatment is applied to the case of a $40M_{\odot}$ star. We adopt 255 spatial zones for lagrangian mass coordinate and 14 energy zones and 6 angle zones for the neutrino distribution function. The 4 species of neutrinos are treated separately as ν_e , $\bar{\nu}_e$, $\nu_{\mu/\tau}$ and $\bar{\nu}_{\mu/\tau}$. Here $\nu_{\mu/\tau}$ denotes the neutrinos of μ - and τ -types and $\bar{\nu}_{\mu/\tau}$ denotes the anti-neutrinos of μ - and τ -types. The other details of methods can be found in (Sumiyoshi et al. 2005).

We remark that the exact treatment of ν -radiation hydrodynamics in general relativity is essential to describe the evolution including compact objects and to predict the neutrino emission in the dynamical situation. The general relativity plays a dominant role to trigger the collapse of proto-neutron star to black hole. The hydrodynamical treatment is necessary to describe the accretion of material onto a shrinking central core and the neutrinos mainly emitted during this accretion phase being different from the quasi-static evolution of proto-neutron stars by the Henyey-type treatment.

The exact treatment of general relativistic ν -radiation hydrodynamics is possible only under the spherical symmetry at the moment (See, however, Buras et al. 2003, 2006; Livne et al. 2004, for efforts on multi-dimensional calculations). We note that the spherically symmetric models considered in this paper may correspond to the branch extending from the faint supernovae that are suggested to be the outcome of the collapse of slowly rotating massive stars (Nomoto 2005). On the other hand, multi-dimensional simulations of ν -radiation hydrodynamics are required to reveal the black hole formation in rapidly rotating massive stars and its possible consequence as hypernovae and/or gamma ray bursts, which are, however, beyond the scope of the current study.

2.2. Input Physics

2.2.1. Equation of state

We use the two sets of supernova EOS which are the standard in recent supernova simulations. The EOS by Lattimer and Swesty (LS-EOS) (Lattimer & Swesty 1991), which has been a conventional choice, is based on the compressible liquid drop model for nuclei together with dripped nucleons. The density dependence of EOS for infinite matter is assumed to take a form for the Skyrme-type effective interactions, which are often used in non-relativistic nuclear many body calculations of nuclear structures. The parameters are determined by the bulk properties at the saturation. The EOS by Shen et al. (SH-EOS) (Shen et al. 1998), which is relatively new, is constructed by the relativistic mean field (RMF) theory along

with a local density approximation. The RMF theory is based on the relativistic nuclear many body frameworks (Brockmann & Machleidt 1990) and has been successfully applied to the studies of nuclear structures and dense matter (Serot & Walecka 1986). It is to be noted that the nuclear interactions to derive SH-EOS are constrained by the properties of unstable nuclei (Sugahara & Toki 1994), which are available recently in radioactive nuclear beam facilities in the world. For example, the neutron skin thickness of neutron-rich nuclei, which is sensitive to the nuclear symmetry energy, is well reproduced for isotopes of light nuclei (Suzuki et al. 1995; Sugahara et al. 1996).

The two sets of supernova EOS are different from each other, reflecting the characteristic of the nuclear theoretical frameworks and the inputs of nuclear data used to constrain the EOS. The relativistic frameworks tend to provide a stiff EOS as compared with the non-relativistic frameworks. The density dependence of symmetry energy tends to be strong in the relativistic frameworks (See, for example, Sumiyoshi et al. 1995b). The incompressibility and symmetry energy of SH-EOS are 281 MeV and 36.9 MeV, respectively. It is to be noted that those values in SH-EOS are not inputs to determine the interactions, but the outcome after the fitting of nuclear interactions to nuclear data of nuclei including neutron-rich ones. For LS-EOS, we adopt the set of 180 MeV for the incompressibility among three choices. The EOS set of this value has been popularly used in most of numerical simulations so far. The symmetry energy of LS-EOS is 29.3 MeV. When those two sets of EOS are adopted for cold neutron stars, the maximum masses are $1.8M_{\odot}$ and $2.2M_{\odot}$ for LS-EOS and SH-EOS, respectively, due to the difference of stiffness. This difference is essential in discussing different maximum masses of proto-neutron stars in numerical simulations. Note that the proto-neutron stars contain more leptons and are hotter than ordinary neutron stars, and therefore, the maximum mass of the former is not the same as for the latter.

As we will demonstrate in § 4, the density and temperature in proto-neutron stars collapsing to black holes become extremely high beyond the range of EOS originally provided in the table. We have extended the EOS table by calculating the necessary quantities according to the original formulation of RMF for SH-EOS (Sumiyoshi et al. 1995a). The corresponding EOS table for LS-EOS is prepared by using the subroutine provided by Lattimer and Swesty for public use. The simple extrapolation of EOS to these extremely high density and temperature, where the applicability of the nuclear many body frameworks with only the nucleonic degree of freedom is doubtful, is apparently oversimplification. However, since this is the first comparison of different EOS's in the rapid black hole formation from the massive star, we adopt the simplest extension of the currently available sets of EOS. There may be the appearance of hyperons, possible condensations of mesons and phase transitions to quarks and gluons at these high density and temperature. They are the targets of upcoming numerical simulations.

2.2.2. Weak interaction rates

We adopt the same set of weak interaction rates as in the previous study on $15M_{\odot}$ star (Sumiyoshi et al. 2005) to facilitate comparisons and numerical checks. The basic set of reaction rates follows the standard formulation of Bruenn (1985). In addition, the plasmon process and the nucleon-nucleon bremsstrahlung are included (Sumiyoshi et al. 2005). The latter reaction has been shown to be an important process as a source of $\nu_{\mu/\tau}$ and $\bar{\nu}_{\mu/\tau}$ from the proto-neutron star (Burrows et al. 2000; Suzuki 1993). The recent developments of neutrino-matter interactions (Burrows et al. 2006) and electron-capture rates (Langanke & Martínez-Pinedo 2003) will be implemented in future. One should be reminded that the details of neutrino signals from the black hole formation may be modified by these updated neutrino reaction rates and further scrutiny. We will demonstrate, however, that the whole dynamics is controlled dominantly by the accretion and the general feature of neutrino emission reflects largely the difference of EOS rather than the minutes of neutrino rates.

2.3. Initial Model

We adopt the presupernova model of $40M_{\odot}$ by Woosley & Weaver (1995). This is the most massive model in the series of their presupernova models and contains an iron core of $1.98M_{\odot}$. Their presupernova model of $15M_{\odot}$, which is the *standard* for recent supernova studies, contains an iron core of $1.32M_{\odot}$ by contrast. The large size of the iron core in the current model warrants the black hole formation without explosion as its fate. We use the profile of central part of the presupernova model up to $3.0M_{\odot}$ in baryon mass coordinate, large enough to describe the accretion of material for a long time.

2.4. Criterion for black hole formation

The general relativistic formulation for the numerical code is based on the metric of Misner & Sharp (1964). In order to track down the formation of black hole, we use the apparent horizon, following the numerical studies of black hole formations from supermassive stars by Nakazato et al. (2006). The apparent horizon exists when the relation

$$\frac{U}{c} + \Gamma \leq 0 \quad (1)$$

or equivalently

$$r \leq r_g \quad (2)$$

is satisfied, where U is the radial fluid velocity and Γ is the general relativistic gamma factor (Yamada 1997, for the definitions). The Schwarzschild radius is defined by

$$r_g = \frac{2GM_g(r)}{c^2} \quad (3)$$

where $M_g(r)$ denotes the gravitational mass inside the radius r . In the current study, we terminate the numerical simulations soon after the formation of the apparent horizon because of possible numerical errors and instability. In order to follow the evolution in a stable manner up to the final moment of the fade-out of neutrino emissions, we need to apply the singularity-avoiding scheme as in Baumgarte et al. (1995). We stress that the main aim of our study is to clarify the dynamics from the beginning of collapse up to the black hole formation through the accretion of outer envelopes as well as the major part of the neutrino signal during this period and, most importantly, their dependence on the EOS.

3. Numerical Results

We present the numerical results for the two models studied with Shen’s EOS and Lattimer-Swesty EOS, which are hereafter denoted by SH and LS, respectively. We start with the outline of the whole evolutions of the two models (§ 3.1) and discuss each stage from the core collapse, bounce (§ 3.2), shock propagation, proto-neutron star evolution (§ 3.3) to the formation of black hole (§ 3.4). We present the results on the distributions and emissions of neutrinos in § 3.5 and 3.6.

3.1. Outline of evolution

Figs. 1 and 2 show the radial trajectories of mass elements as a function of time after core bounce (t_{pb}) in models SH and LS. The trajectories are plotted for each $0.02M_\odot$ in baryon mass coordinate. Thick lines denote the trajectories for $0.5M_\odot$, $1.0M_\odot$, $1.5M_\odot$, $2.0M_\odot$ and $2.5M_\odot$. After the gravitational collapse of central iron core of the initial model, the core bounce occurs at central densities just above the nuclear matter density as in the ordinary core-collapse supernovae. The time at the core bounce from the start of the simulation is 0.357 sec and 0.333 sec, respectively, in models SH and LS.

The shock wave is launched by the core bounce and propagates beyond 100 km in both models. Because of the significant amount of matter accretion, the shock wave starts recession at $t_{pb} \sim 100$ ms and becomes the accretion shock above the central object just born at center. The proto-neutron star is formed after bounce and gradually contracts from

the beginning. The whole proto-neutron star shrinks due to the increase of mass by the accretion. This tendency is striking in model LS, which adopts a softer EOS, having large gradients of radial trajectories in the central part. Note that the rate of accretion is similar in the two models as we can see from the trajectories in the outer core above 100 km.

The gravitational collapse of the proto-neutron star occurs when the mass of proto-neutron star exceeds the maximum mass for the stable configurations of lepton-rich, hot neutron stars. The re-collapse proceeds dynamically within a few msec and the central object becomes exceedingly compact, leading to the formation of black hole. The dynamical collapse to the black hole occurs at $t_{pb}=1.34$ s and 0.56 s, respectively, in models SH and LS.

3.2. Initial collapse and bounce

The gravitational collapse of central iron core from the initial model occurs in a similar way as in the ordinary core-collapse supernovae (e.g. $15M_{\odot}$ model). The electron captures on free protons and nuclei proceed to reduce the lepton fraction until neutrino trapping. The neutrinos (ν_e) are trapped at high densities ($\sim 10^{12}$ g/cm³) and contribute to build up the bounce core. During the collapse, the compositional difference between the two models can be seen as we have found in the case of $15M_{\odot}$ model. In fact, model SH tends to reduce electron captures, having a smaller free proton fraction than model LS.

We define the core bounce ($t_{pb}=0$ s) as the time when the central density reaches the maximum in this stage. The central density at bounce is 3.2×10^{14} g/cm³ and 4.1×10^{14} g/cm³ in models SH and LS, respectively. After a slight expansion at bounce, the central densities gradually increase owing to the contraction of proto-neutron stars.

The profiles of lepton fractions at bounce are shown in Fig. 3. The lepton fraction and electron fraction at center in SH is 0.35 and 0.30, respectively. The corresponding values in LS are smaller, but the difference between the two models is ~ 0.01 . The modest difference leads to a small difference of the bounce cores. Fig. 4 displays the velocity profiles at bounce in the two models. The size of bounce core in SH is slightly larger than that in LS, but the difference is again small $\leq 0.02M_{\odot}$. The radial position of shock wave in SH is 11 km and that in LS is only $\sim 2\%$ smaller at their formations. Accordingly, the propagations of shock wave in the early phase (up to $t_{pb} \sim 100$ ms) are similar to each other in the two models.

3.3. Rapid formation of proto-neutron star

The shock wave propagates through the iron core, but it never overcomes the ram pressure of falling material. It stalls at ~ 150 km and turns into the recession due to the substantial influence of the accretion. In fact, the material of about $1M_{\odot}$ falls down within 100 ms after bounce in both models. The shock wave reaches $1.6M_{\odot}$ at $t_{pb}=100$ ms and the central core below the shock wave acquires a typical neutron star mass already. Although the outer part of the central core is not yet hydrostatic, the proto-neutron star has been formed already in terms of mass. This is much faster than the case of ordinary core-collapse supernovae, in which it takes 300–400 ms to acquire the enough mass ($\sim 1.5M_{\odot}$ in baryon mass) for proto-neutron stars.

We show in Figs. 5 and 6 the profiles of density and temperature in the two models at $t_{pb}=0, 100, 300$ and 500 ms. The rapid growth of proto-neutron star masses is evident with the mass over $2M_{\odot}$ in 500 ms after bounce. The difference of masses in the two models are within $0.03M_{\odot}$, reflecting the initial difference in the size of bounce cores and the similarity of the accretion rates in the two models. The densities inside proto-neutron star in model LS after $t_{pb}=300$ ms become higher than those in model SH because of the softness of LS-EOS. The central density in model LS exceeds 10^{15} g/cm³ at $t_{pb}=500$ ms. Owing to the compression of dense matter, the temperature inside becomes high, peaked at $0.6\text{--}0.7M_{\odot}$, where the heating due to the passage of shock wave is significant. The peak temperatures reach 51 MeV and 85 MeV at $t_{pb}=500$ ms in models SH and LS, respectively. This large difference is caused by the faster compression in model LS than in model SH. We remark that the peak values of entropy per baryon in the two models are almost equal.

The time evolutions of the baryon mass inside the proto-neutron star in the two models are shown in Fig. 7. They are surprisingly similar after bounce, which means that the accretion rates are similar in the two models. In model LS, the baryon mass reaches $2.10M_{\odot}$ at $t_{pb}=0.56$ s and exceeds the maximum mass for the stable configurations, leading to the dynamical collapse to the black hole. In model SH, it increases further up to $2.66M_{\odot}$ at $t_{pb}=1.34$ s. For comparison, we plot the corresponding baryon mass of the proto-neutron star taken from the numerical result of the gravitational collapse of a $15M_{\odot}$ star with SH-EOS (Sumiyoshi et al. 2005) as an example of massive stars, which are supposed to lead to ordinary core-collapse supernovae. The growth of proto-neutron star is much faster in the case of the $40M_{\odot}$ star than in the case of the $15M_{\odot}$ star. This means that the accretion rate in the current models of $40M_{\odot}$ is considerably higher than that in the canonical model of $15M_{\odot}$. The accretion rate is $\sim 1M_{\odot}/\text{s}$ in the current models at $t_{pb}=0.4$ s while it is $\sim 0.2M_{\odot}/\text{s}$ for $15M_{\odot}$ model. This large accretion rate makes the astrophysical events from the $40M_{\odot}$ stars unique, having a rapid contraction of proto-neutron stars and a quick formation of

black hole. This is clearly different from the delayed scenario of black hole formation after the cooling of proto-neutron stars from ordinary supernovae.

3.4. Re-collapse and formation of black hole

In Figs. 8, 9 and 10, we display the profiles of density, temperature and velocity at final stages up to the black hole formation. Here t_{bh} denotes the time before the black hole formation. As sample snapshots, we plot the profiles at the beginning of re-collapse ($t_{bh}=-8.2$ ms and -1.0 ms for SH and LS, respectively) by dashed lines and the profiles at the time ($t_{bh}=-0.14$ ms and -0.19 ms for SH and LS, respectively) when the central density reaches $\sim 2 \times 10^{15}$ g/cm³ (near the maximum density in the original table of SH-EOS) by long-dashed lines. The timing of the snapshot of the re-collapse is chosen to be when the velocity just behind the shock wave exceeds -2×10^8 cm/s for practical reasons. The profiles at the formation of apparent horizon are shown by solid lines. For model SH, we plot also the profile at $t_{pb}=1$ s by dot-dashed lines.

In both models, the density in the whole proto-neutron stars increases within short times during the re-collapse, while the baryon mass of proto-neutron stars does not change so much. The central density reaches $\sim 10^{16}$ g/cm³ at the end of computations. The temperature increases beyond 100 MeV during the re-collapse and reaches ~ 200 MeV at the peak position for model LS and a lower value for model SH. The re-collapse proceeds dramatically having the velocity increase from $\sim 10^6 - 10^8$ cm/s at the beginning, to $\sim 10^9$ cm/s within 1 – 10 ms. The velocity eventually exceeds $\sim 10^{10}$ cm/s by the time of black hole formation.

The general relativistic factors, Γ and e^ϕ , at the time of formation of apparent horizon are shown in Fig. 11. The general relativistic gamma factor, Γ , has the minimum around $1.5M_\odot$. The large negative values for the velocity affects the location of apparent horizon, which is defined by the condition, $U/c + \Gamma = 0$ (see the definition in § 2.4). The apparent horizon is formed at $\sim 1.2M_\odot$ (~ 5 km in radius) in model SH and at $\sim 1.3M_\odot$ (~ 5 km in radius) in model LS.

3.5. Neutrino distributions

We show the distributions of leptons in model SH at $t_{pb}=100, 500$ msec and $t_{bh}=0$ (black hole formation) in Fig. 12. The number fraction (number per baryon), Y_i , is defined by the ratio, n_i/n_B , where n_i and n_B denote the number densities of particle i and baryon, respectively. The (electron-type) lepton fraction, Y_L , which is defined by the sum of net

electron fractions, $Y_{e-}-Y_{e+}$, and net (electron-type) neutrino fractions, $Y_{\nu_e}-Y_{\bar{\nu}_e}$, is shown by solid line. The (net) electron fraction, Y_e , neutrino fractions for ν_e , $\bar{\nu}_e$ and $\nu_{\mu/\tau}$ are shown by dashed, dotted, dot-dashed and dot-dot-dashed lines, respectively.

After the core bounce, the neutronization of matter proceeds after the passage of shock wave and the electron fraction decreases drastically like in the case of the proto-neutron star formation in ordinary supernovae. A trough of the lepton fraction is formed between the outer edge of inner core and the shock position by $t_{pb}=100$ msec and persists until the black hole formation. The profile of the lepton fraction is not changed much while the shape becomes wider according to the shock propagation. The fraction of ν_e , which has been produced during the collapse and trapped inside the inner core, decreases during the evolution. The $\bar{\nu}_e$ fraction increases initially in the outer core and prevails in the whole core at the end. Because of the appearance of $\bar{\nu}_e$'s, the lepton fraction is smaller than the electron fraction at $t_{bh}=0$. The ν_e and $\bar{\nu}_e$ fractions are determined by the conditions for beta equilibrium including neutrinos and their evolution is driven by the decrease of chemical potential, μ_ν , for electron-type neutrinos. Since the relation among the chemical potentials for electrons, protons and neutrons holds as $\mu_\nu = \mu_e + \mu_p - \mu_n$ through the quasi-chemical equilibrium, the reduction of μ_ν occurs by the compression of matter leading to the black hole formation. This is because the compression leads to the increase of μ_n and the decrease of μ_p by the increasing effect of symmetry energy at very high densities. The decrease of μ_ν (actually to negative values) drives a shift from the dominance of ν_e to that of $\bar{\nu}_e$ under the beta equilibrium. The $\nu_{\mu/\tau}$ and $\bar{\nu}_{\mu/\tau}$ neutrinos are produced by pair processes and, therefore, appear mainly in the region with non-degenerate electrons.

The diffusion of neutrinos trapped inside the proto-neutron star is actually slow and the emission of neutrinos is mainly driven by the accretion. In Fig. 13, we show the profiles of neutrino luminosities at $t_{pb}=1$ sec in model SH as a function of radius, for example. The luminosities increase stepwise at ~ 20 km, which corresponds to the outer edge (surface) of proto-neutron star. This is because the cooling of material is maximum there producing neutrinos by the electron and positron captures on nucleons and by the pair (electron and positrons) annihilation processes. The accreting matter falls down to the surface after being heated by shock wave and compression, and then cools down by emitting neutrinos while it settles down hydrostatically. In order to demonstrate the neutrino emitting region, we show, in Fig. 14, the positions of neutrinosphere at $t_{pb}=1$ sec in model SH as a function of neutrino energy. We define the neutrinosphere where the optical depth becomes $2/3$ for the neutrino with a specific energy. The neutrinospheres are located at $20\sim 200$ km, where the accreting matter cools down by emitting neutrinos. Some of the high energy neutrinos are reabsorbed by falling material and are not free-streaming up to ~ 200 km. It is to be noted that the neutrinosphere for $\nu_{\mu/\tau}$'s is located in the innermost part while the ones for ν_e and

$\bar{\nu}_e$ in the outer part. This is because $\nu_{\mu/\tau}$'s interact only through neutral currents whereas ν_e 's and $\bar{\nu}_e$'s interact through both neutral and charged currents. This difference leads to the hierarchy of the average energies for different neutrino species that we will see in neutrino signals, since the temperature becomes higher as one goes inwards.

3.6. Neutrino signals

In Figs. 15 and 16, we show the average energies and luminosities of ν_e , $\bar{\nu}_e$ and $\nu_{\mu/\tau}$ as a function of time (t_{pb}) for the two models. These quantities are the ones measured at the outermost grid point (~ 6000 km). The average energy presented here is defined by the rms value, $\langle E_\nu^2 \rangle^{\frac{1}{2}}$. The plots for $\bar{\nu}_{\mu/\tau}$ are not shown since they show no significant difference from the ones for $\nu_{\mu/\tau}$. We will only discuss $\nu_{\mu/\tau}$ and will not mention $\bar{\nu}_{\mu/\tau}$ hereafter.

Around the core bounce ($t_{pb} = -0.1 \sim 0.1$ s), the time profiles of average energies and luminosities are similar to those for ordinary supernovae. There is a distinctive peak due to the neutronization burst in the luminosity of ν_e . The rise of the luminosities of $\bar{\nu}_e$ and $\nu_{\mu/\tau}$ right after bounce occurs owing to the thermal production of neutrinos. The peak of average energies around the core bounce appears as a result of heating by the passage of shock wave. The behaviors in two models SH and LS are similar to each other up to $t_{pb} \sim 0.1$ s.

After that, the average energies increase toward the black hole formation, reflecting the temperature increase. This tendency is more evident in model LS since the contraction of proto-neutron star is faster and the resulting temperature is higher. The average energy of $\nu_{\mu/\tau}$ increases most prominently among three species, having the neutrinosphere at the innermost. The average energies of ν_e and $\bar{\nu}_e$ are rather close to each other because their neutrinospheres locate at similar positions, which are determined by charged current reactions on mixture of neutrons and protons. It is remarkable to see that the average energies rise continuously up to the end and the increase amounts to a factor of two to three from the value right after the bounce. This behavior of neutrino emission is different from the one seen usually in the numerical simulations of ordinary supernovae. In the latter, the proto-neutron star is more static and does not contract so much because the accretion ceases soon after the bounce. Therefore, the increase of average energies after bounce is a clear signal that tells us the evolution toward the black hole formation.

The luminosities after the neutronization burst also increase toward the black hole formation. This is in accord with the increase of accretion luminosity, especially for ν_e and $\bar{\nu}_e$. The accretion luminosity is proportional to $GM\dot{M}/r$, where M and r denote the mass and radius, respectively, of the proto-neutron star discussed in § 3.3. While the accretion

rate, \dot{M} , stays roughly constant, the radius decreases dramatically like the shock positions in Figs. 1 and 2 toward the end. The actual neutrino luminosities, which are a portion of the available energy obtained by the accretion, depend on the cooling processes. The cooling by ν_e and $\bar{\nu}_e$ emissions proceeds through the electron and positron captures on nucleons in hot accreting matter. Since the matter is non-degenerate and the electron fraction is ~ 0.5 containing both neutrons and protons equally, the ν_e and $\bar{\nu}_e$ luminosities are nearly equal. The $\nu_{\mu/\tau}$ luminosities are determined by the pair process (annihilation of electron-positron pairs), and, therefore, reflect the temperature change at the neutrinosphere for $\nu_{\mu/\tau}$'s.

It is to be noted that the computations of neutrino burst are terminated at the formation of apparent horizon in this study. After this moment, the neutrinosphere will be swallowed by the horizon in a fraction of millisecond and the major neutrino emissions cease at this point. Since neutrinos emitted just at the neutrinosphere travel over ~ 6000 km to the observing point set at the outer boundary of the computation domain, the neutrino signals last for ~ 20 msec more, in reality, from the end point in the current figures. The last part of neutrino signals will be affected more clearly by general relativity, e.g. as the energy red shift (Baumgarte et al. 1996a). Such detailed information of neutrino spectra is valuable to examine general relativistic effects and to constrain neutrino masses (Beacom et al. 2001). In order to predict the final moment of neutrino emission, however, one needs to implement a scheme to avoid both coordinate- and real singularities (Baumgarte et al. 1995), which will be postponed to the future work. The scope of the current study is to reveal the general feature of the evolution from the massive progenitor to the black hole. It is the difference in the duration of proto-neutron star era and associated neutrino bursts that we aim to clarify using the two realistic equations of state of dense matter.

In Fig. 17, we show the time evolutions of energy spectra at the outermost grid point for model SH. It is apparent that the spectra become harder during the evolution toward the black hole formation as the average energies and the luminosities evolve (see also Figs. 15 and 16). At $t_{pb}=100$ ms, the peak of spectrum is located around 10~20 MeV having the same hierarchy as in the average energies. The peak is shifted to higher energies (~ 20 MeV) and the spectral shapes become similar among three neutrino species at $t_{pb}=500$ ms. The spectra for ν_e and $\bar{\nu}_e$ are similar to each other due to the comparable production mechanisms as discussed above. The spectra for $\nu_{\mu/\tau}$'s become rapidly harder further toward $t_{bh}=0$ reflecting higher temperatures of the central object.

We compare the energy spectra for models SH and LS and found that the difference is minor as long as we compare them at the same timing after bounce. The spectra at $t_{pb}=100$ ms for LS is quite similar to the ones shown in (a) of Fig. 17. We show the comparison at $t_{pb}=500$ ms in Fig. 18. The luminosities for model LS are slightly higher than those for

model SH. The $\nu_{\mu/\tau}$ spectra for model LS are harder than those for model SH, while the ν_e and $\bar{\nu}_e$ spectra look similar for both models. These differences arise from the fact that the proto-neutron star in model LS at $t_{pb}=500$ ms is already close to the state of the maximum mass whereas the model SH waits for the further evolution.

4. Implications for EOS studies

Here we describe the temperature and density regimes that the stellar matter experiences during the evolution to the black hole formation and discuss their implications for the further development of EOS. In Figs. 19 and 20, we plot the density and temperature of matter along the trajectory for a fixed baryon mass coordinate as a function of time after bounce for the two models. At the center (Fig. 19), the density increases quickly before the core bounce and gradually thereafter toward the re-collapse. By the time of re-collapse, the density reaches 10^{15} g/cm³, which is 3 times the normal nuclear matter density. The temperature exceeds 10 MeV at bounce, and gradually increases beyond 30 MeV toward the re-collapse. The final sharp increases we can see in figures are due to the dynamical collapse to the black hole within a millisecond. We remark that the behavior before the sharp increase is important to determine the trigger of the gravitational collapse at the maximum mass during the evolution of proto-neutron stars. In Fig. 20, we show the case for $0.6M_{\odot}$ in baryon mass coordinate, where the entropy peak is formed by the passage of shock wave. In this case, the temperature increases fast and becomes much higher than at the center. The temperature reaches 80 MeV for SH (90 MeV for LS) before the re-collapse and the density exceeds twice the normal nuclear matter density. These high density and temperature regimes are important to study the rapid collapse of proto-neutron stars.

As we described in § 2.2.1, we adopt the equations of state with only the nucleonic degree of freedom in the current study. For high densities and temperatures we have seen above, more massive baryons including strangeness may appear and the quark degree of freedom becomes essential to describe the dense and hot matter. An emergence of new degrees of freedom will lead to the softening of equation of state and, therefore, it makes the maximum mass of proto-neutron star smaller and the re-collapse earlier. In this sense, the current result gives the maximum duration of proto-neutron star era. Still, it is astonishing that we see a large difference even within the nucleonic EOSs. The current results are also the basis to explore when the exotic phases of dense matter appear during the evolution. The determination of the end point of neutrino burst will be important to put a constraint on the phase transitions of dense matter. A shorter burst than the current prediction may suggest the existence of new phases on the density-temperature trajectories studied here.

It is certainly important to constrain the nucleonic EOS further as a firm basis as well as to perform numerical simulations with the extended EOS table with exotic phases. The systematic study on the hyperon and/or quark EOSs covering a wide range of environment and on the associated neutrino reactions is currently under way.

In the current study, we have used the incompressibility of 180 MeV among the three choices in LS-EOS. If we use LS-EOS with the higher incompressibility of 220 MeV, the duration of neutrino signal will become longer than in the current case of 180 MeV and the difference between LS-EOS and SH-EOS will be smaller than for the results we have shown. Since the characteristics of EOS depends not only on the incompressibility but also on the symmetry energy, adiabatic index and other factors at high densities, it would be interesting to extract the dependence on the incompressibility alone by numerical simulations using LS-EOS with the higher incompressibility.

5. Summary

We study the gravitational collapse of a non-rotating massive star of $40 M_{\odot}$ resulting in the black hole formation. Adopting the two different sets of realistic equation of state (EOS) of dense matter, we perform the numerical simulations of general relativistic ν -radiation hydrodynamics. We reveal the influence of EOS on the core bounce, the shock propagation, the formation of proto-neutron star and the ensuing re-collapse to black hole together with neutrino emissions during the evolution. Following the core bounce and shock stall, the accretion of material from outer layers causes the rapid increase of the mass of nascent proto-neutron star. Accordingly, the proto-neutron star immediately starts shrinking within 100 msec after bounce. The speed of contraction depends predominantly on the adopted EOS, and the density and temperature of the proto-neutron star become very high as compared with those for ordinary proto-neutron stars in successful supernovae. We find that the duration of proto-neutron star era is clearly different depending on the EOS, which determines the maximum mass of proto-neutron stars. Due to the gravitational instability beyond the maximum mass, the fat proto-neutron star collapses again at 0.56 s and 1.34 s after bounce for the models with LS-EOS and SH-EOS, respectively. The apparent horizon is formed within ~ 1 msec. The black hole is formed much more quickly after the initial collapse of massive star than in the delayed scenarios. The resulting ν emissions during the dynamical evolution are distinctive as compared with the neutrino signals not only from ordinary supernovae but also from the delayed collapse models. The ever increasing average energies of neutrinos and the sudden termination of neutrino signals are the clear evidence of the rapid black hole formation from massive stars considered here. Although the increasing

feature of energy can be seen also in some models of successful explosions, it is more robust in this case due to the lasting intense accretion. In addition, the duration of ν emissions can be used to constrain the stiffness of EOS at high density and temperature. A softer EOS or an early occurrence of the phase transition to exotic phases may lead to a shorter neutrino burst. Further studies concerning the dependences on progenitor models and the EOS with hyperon or quarks are necessary to provide the templates for the neutrino signal of black hole formation and will be reported in separate papers. It would be interesting to study the black hole formation from rotating massive stars since the rotation will modify the formation time and the associated neutrino signal, which may contain the contributions from accretion disks. A terrestrial detection of neutrino bursts from this type of collapse of massive stars in future will reveal the rapid black hole formation and will put a new constraint on the EOS at extreme conditions.

The authors are grateful to H. Shen, K. Oyamatsu, A. Ohnishi, C. Ishizuka and H. Toki for the collaborations on the tables of equation of state for supernova simulations. K. S. is grateful to T. Maruyama and S. Chiba for the arrangement of computing resources at JAEA. We thank M. Liebendorfer, K. Nakazato, S. Fujimoto and T. Kajino for fruitful discussions and keen comments. The numerical simulations were performed at NAO (wks06a, iks13a), JAEA and YITP. This work is partially supported by the Grants-in-Aid for the Scientific Research (15540243, 15740160, 18540291, 18540295) of the MEXT of Japan, Academic Frontier Project and KEK LSSP (06-02).

REFERENCES

- Baumgarte, T. W., Janka, H.-T., Keil, W., Shapiro, S. L., & Teukolsky, S. A. 1996a, *Astrophys. J.*, 468, 823
- Baumgarte, T. W., Shapiro, S. L., & Teukolsky, S. A. 1995, *Astrophys. J.*, 443, 717
- . 1996b, *Astrophys. J.*, 458, 680
- Beacom, J. F., Boyd, R. N., & Mezzacappa, A. 2001, *Phys. Rev.*, D63, 073011
- Bethe, H. A. 1990, *Rev. Mod. Phys.*, 62, 801
- Bionta, R. M. et al. 1987, *Phys. Rev. Lett.*, 58, 1494
- Brockmann, R. & Machleidt, R. 1990, *Phys. Rev.*, C42, 1965
- Bruenn, S. W. 1985, *Astrophys. J. Suppl.*, 58, 771

- Buras, R., Rampp, M., Janka, H.-T., & Kifonidis, K. 2003, *Phys. Rev. Lett.*, 90, 241101
- . 2006, *Astron. Astrophys.*, 447, 1049
- Burrows, A. 1988, *Astrophys. J.*, 334, 891
- Burrows, A., Reddy, S., & Thompson, T. A. 2006, *Nucl. Phys.*, A777, 356
- Burrows, A., Young, T., Pinto, P., Eastman, R., & Thompson, T. A. 2000, *Astrophys. J.*, 539, 865
- Fryer, C. 1999, *Astrophys. J.*, 522, 413
- Glendenning, N. K. 1995, *Astrophys. J.*, 448, 797
- Heger, A., Fryer, C., Woosley, S., Langer, N., & Hartmann, D. 2003, *Astrophys. J.*, 591, 288
- Hirata, K. et al. 1987, *Phys. Rev. Lett.*, 58, 1490
- Keil, W. & Janka, H.-T. 1995, *Astron. Astrophys.*, 296, 145
- Langanke, K. & Martínez-Pinedo, G. 2003, *Rev. Mod. Phys.*, 75, 819
- Lattimer, J. M. & Swesty, F. D. 1991, *Nucl. Phys.*, A535, 331
- Liebendoerfer, M., Messer, O. E. B., Mezzacappa, A., Bruenn, S. W., Cardall, C. Y., & Thielemann, F.-K. 2004, *Astrophys. J. Suppl.*, 150, 263
- Livne, E., Burrows, A., Walder, R., Lichtenstadt, I., & Thompson, T. A. 2004, *Astrophys. J.*, 609, 277
- MacFadyen, A. & Woosley, S. 1999, *Astrophys. J.*, 524, 262
- Maeda, K. & Nomoto, K. 2003, *Astrophys. J.*, 598, 1163
- Misner, C. W. & Sharp, D. H. 1964, *Phys. Rev.*, B136, 571
- Nakazato, K., Sumiyoshi, K., & Yamada, S. 2006, *Astrophys. J.*, 645, 519
- Nomoto, K. 2005, *ASP Conf. Ser.*, 332, 374
- Pons, J. A., Miralles, J. A., Prakash, M., & Lattimer, J. M. 2001a, *Astrophys. J.*, 553, 382
- Pons, J. A., Reddy, S., Prakash, M., Lattimer, J. M., & Miralles, J. A. 1999, *Astrophys. J.*, 513, 780

- Pons, J. A., Steiner, A. W., Prakash, M., & Lattimer, J. M. 2001b, *Phys. Rev. Lett.*, 86, 5223
- Sato, K. & Suzuki, H. 1987, *Phys. Rev. Lett.*, 58, 2722
- Serot, B. D. & Walecka, J. D. 1986, in *Advances in Nuclear Physics*, ed. J. W. Negele & E. Vogt, Vol. 16 (New York: Plenum Press), 1
- Shen, H., Toki, H., Oyamatsu, K., & Sumiyoshi, K. 1998, *Nucl. Phys.*, A637, 435
- Sugahara, Y., Sumiyoshi, K., Toki, H., Ozawa, A., & Tanihata, I. 1996, *Prog. Theor. Phys.*, 96, 1165
- Sugahara, Y. & Toki, H. 1994, *Nucl. Phys.*, A579, 557
- Sumiyoshi, K., Kuwabara, H., & Toki, H. 1995a, *Nucl. Phys.*, A581, 725
- Sumiyoshi, K., Oyamatsu, K., & Toki, H. 1995b, *Nucl. Phys.*, A595, 327
- Sumiyoshi, K., Yamada, S., Suzuki, H., & Chiba, S. 2006, *Phys. Rev. Lett.*, 97, 091101
- Sumiyoshi, K., Yamada, S., Suzuki, H., Shen, H., Chiba, S., & Toki, H. 2005, *Astrophys. J.*, 629, 922
- Suzuki, H. 1993, in *Proceedings of the International Symposium on Neutrino Astrophysics: Frontiers of Neutrino Astrophysics*, ed. Y. Suzuki & K. Nakamura (Tokyo: Universal Academy Press Inc.), 219
- Suzuki, H. 1994, in *Physics and Astrophysics of Neutrinos*, ed. M. Fukugita & A. Suzuki (Tokyo: Springer-Verlag), 763
- Suzuki, T. et al. 1995, *Phys. Rev. Lett.*, 75, 3241
- Woosley, S. E. & Weaver, T. 1995, *Astrophys. J. Suppl.*, 101, 181
- Yamada, S. 1997, *Astrophys. J.*, 475, 720
- Yamada, S., Janka, H.-T., & Suzuki, H. 1999, *Astron. Astrophys.*, 344, 533

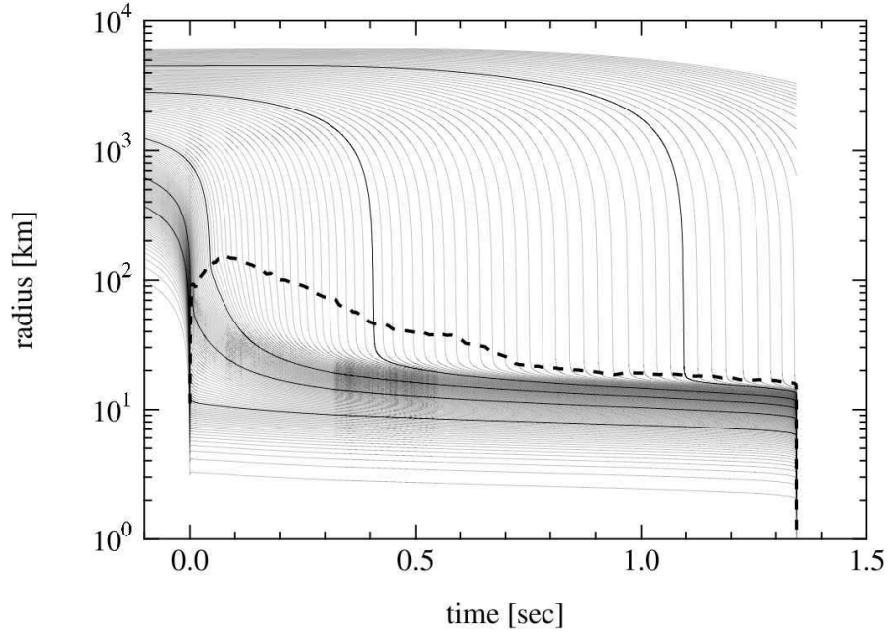


Fig. 1.— Radial trajectories of mass elements of the core of $40M_{\odot}$ star as a function of time after bounce in model SH. The location of shock wave is displayed by a thick dashed line.

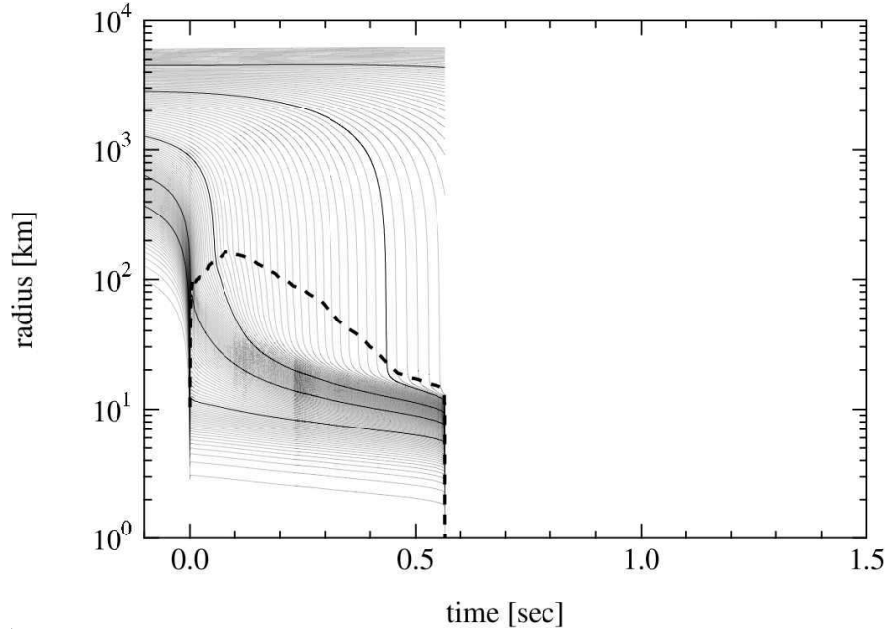


Fig. 2.— Radial trajectories of mass elements of the core of $40M_{\odot}$ star as a function of time after bounce in model LS. The location of shock wave is displayed by a thick dashed line.

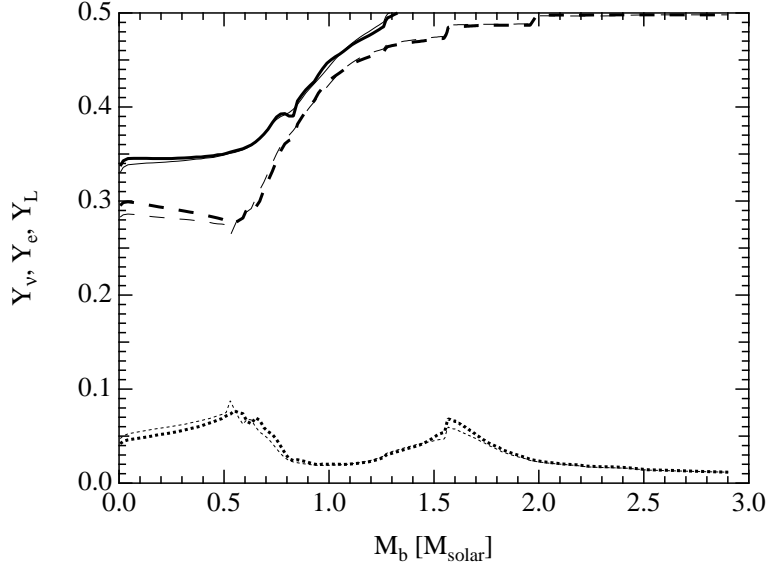


Fig. 3.— Lepton, electron and neutrino (ν_e) fractions at bounce are shown as a function of baryon mass coordinate by solid, dashed and dotted lines, respectively. The results for models SH and LS are shown by thick and thin lines, respectively.

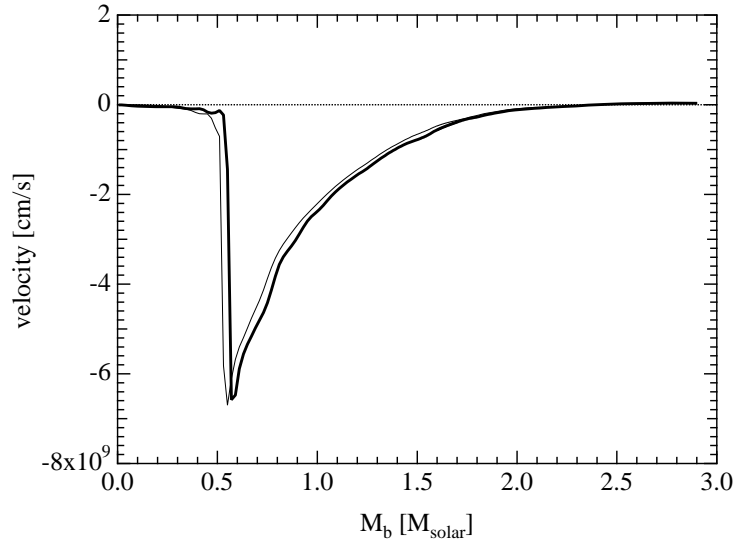


Fig. 4.— Velocity profiles at bounce are shown as a function of baryon mass coordinate. The results for models SH and LS are shown by thick and thin lines, respectively.

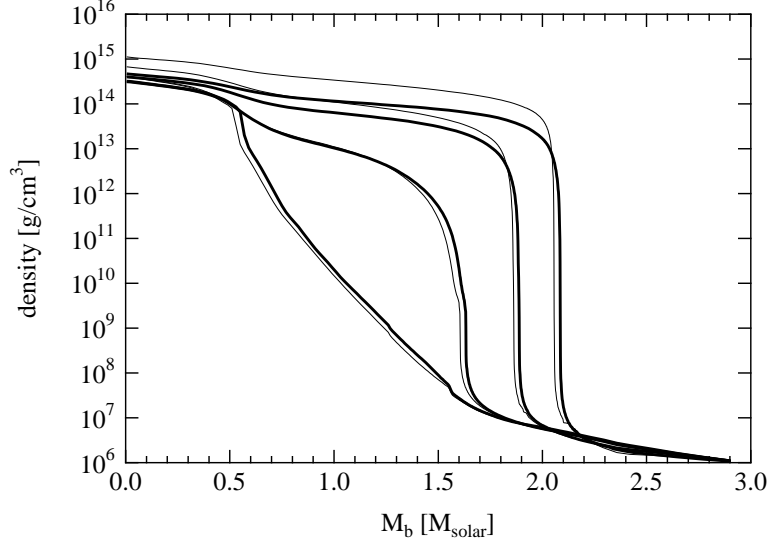


Fig. 5.— Density profiles at $t_{pb}=0, 100, 300$ and 500 ms are shown as a function of baryon mass coordinate. The results for models SH and LS are shown by thick and thin lines, respectively.

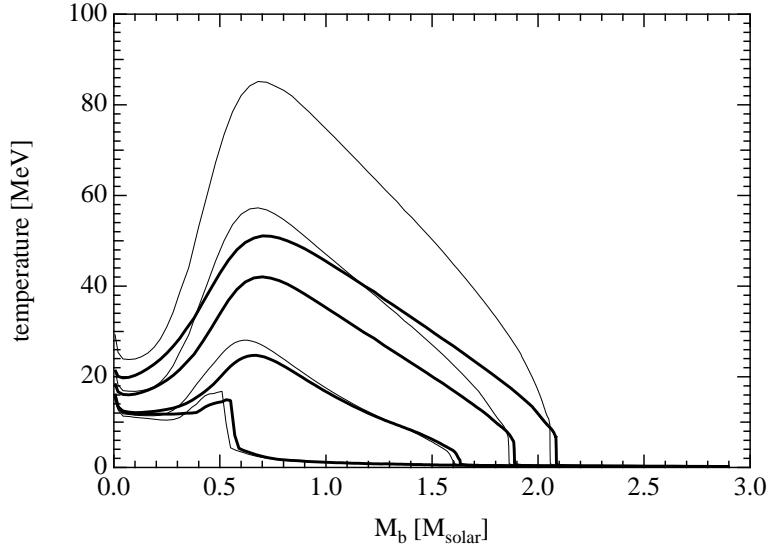


Fig. 6.— Temperature profiles at $t_{pb}=0, 100, 300$ and 500 ms are shown as a function of baryon mass coordinate. The results for models SH and LS are shown by thick and thin lines, respectively.

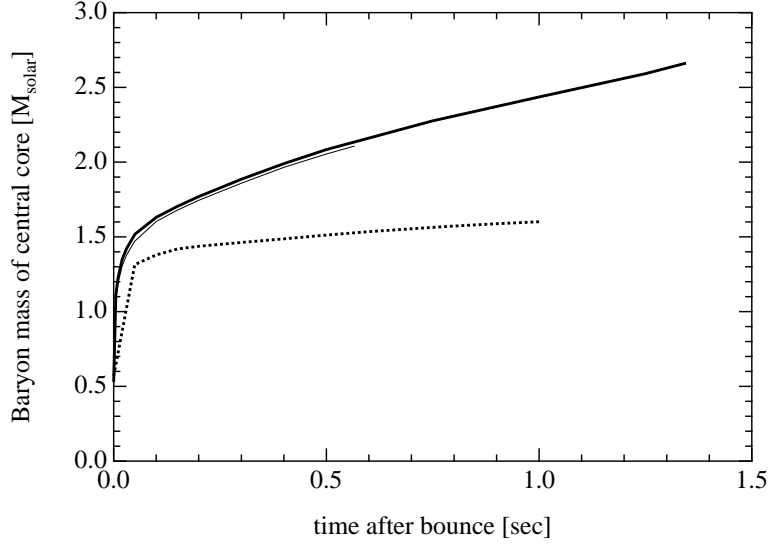


Fig. 7.— Baryon masses of central core (proto-neutron star) in model SH (thick solid line) and LS (thin solid line) are shown as a function of time after bounce. The case of a $15M_{\odot}$ star with SH-EOS is plotted by dotted line for comparison.

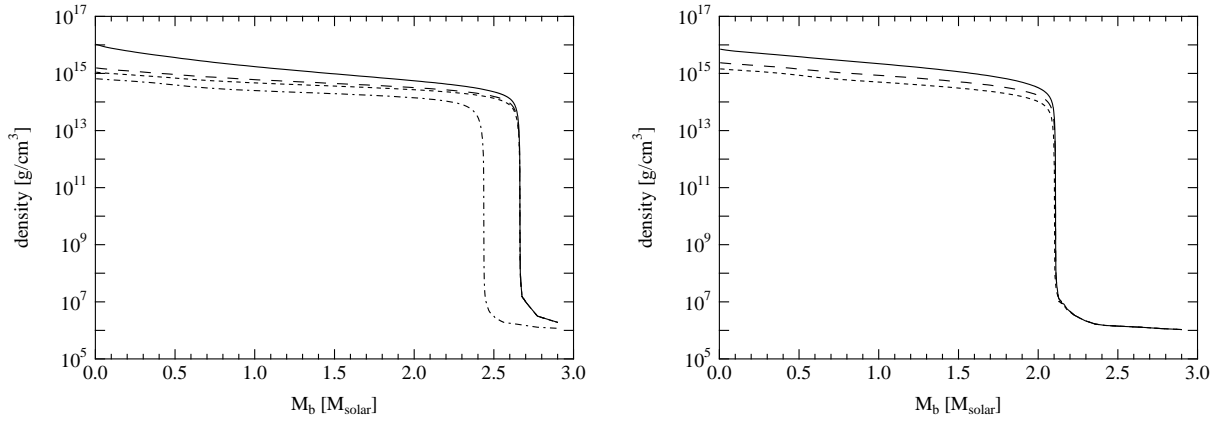


Fig. 8.— Density profiles are shown as a function of baryon mass coordinate in models SH (left) and LS (right). The profiles at the formation of apparent horizon are depicted by solid lines. The profiles at the beginning of re-collapse and at the time when the central density reaches $\sim 2 \times 10^{15} \text{ g/cm}^3$ are depicted by dashed and long-dashed lines, respectively. For model SH, the profile at $t_{pb}=1 \text{ s}$ is shown by dot-dashed line.

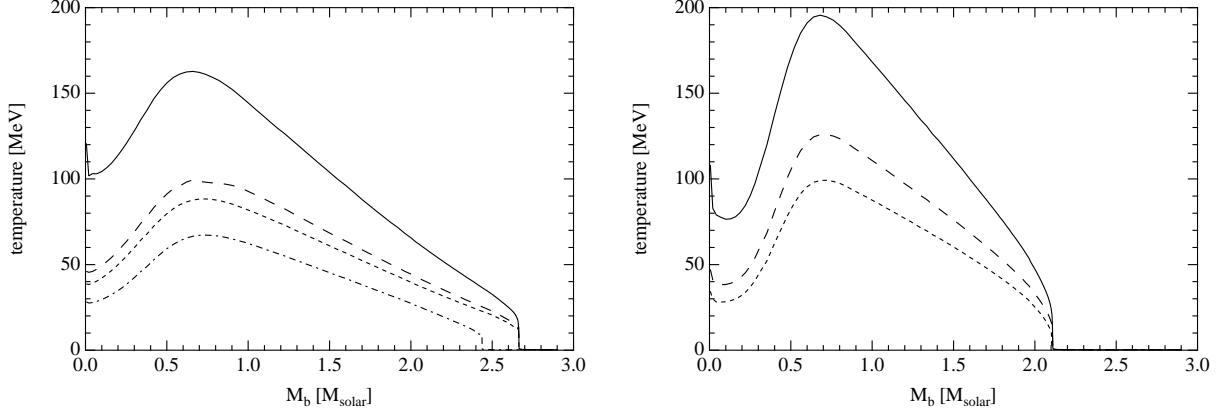


Fig. 9.— Temperature profiles are shown as a function of baryon mass coordinate in models SH (left) and LS (right). The notation is the same as in Fig. 8.

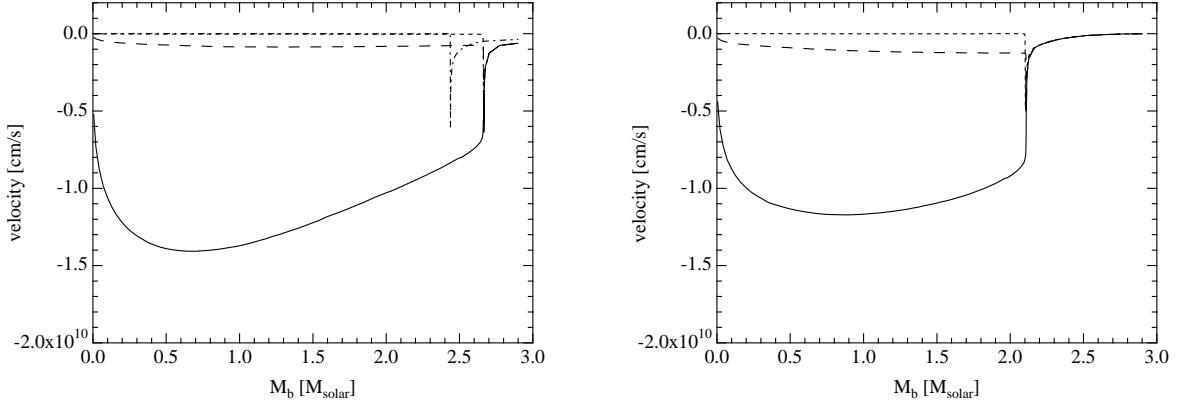


Fig. 10.— Velocity profiles are shown as a function of baryon mass coordinate in models SH (left) and LS (right). The notation is the same as in Fig. 8.

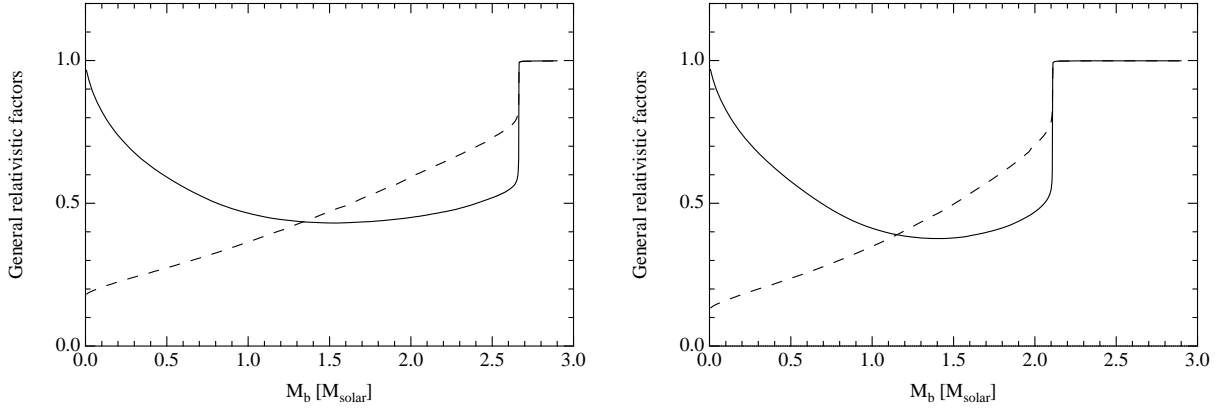


Fig. 11.— General relativistic factors, Γ and e^ϕ , at the formation of apparent horizon are shown as a function of baryon mass coordinate by solid and dashed lines, respectively, in models SH (left) and LS (right).

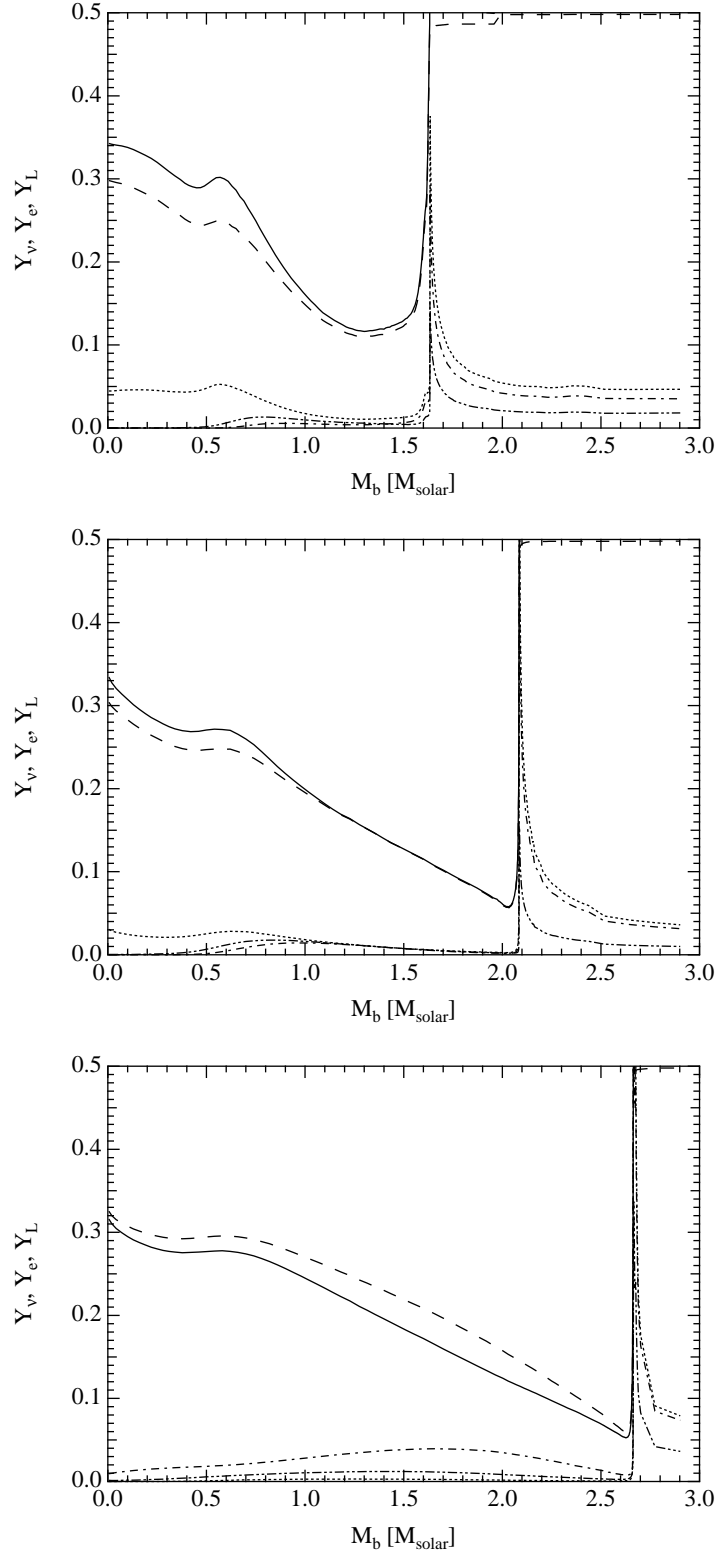


Fig. 12.— Number fractions of leptons, electrons, ν_e , $\bar{\nu}_e$ and $\nu_{\mu/\tau}$ are shown as a function of baryon mass coordinate by solid, dashed, dotted, dot-dashed and dot-dot-dashed lines, respectively, at $t_{pb}=100$ msec (top), $t_{pb}=500$ msec (middle) and $t_{bh}=0$ (bottom) for model SH.

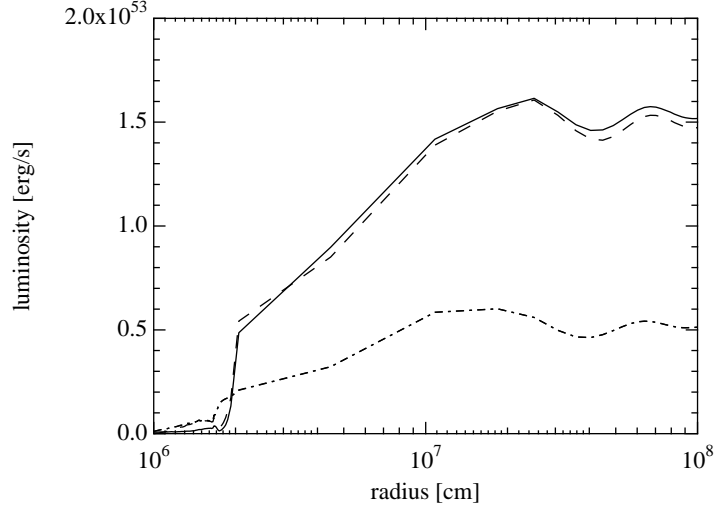


Fig. 13.— Luminosities of ν_e , $\bar{\nu}_e$ and $\nu_{\mu/\tau}$ are shown as a function of radius by solid, dashed and dot-dashed lines, respectively, at $t_{pb}=1$ sec for model SH.

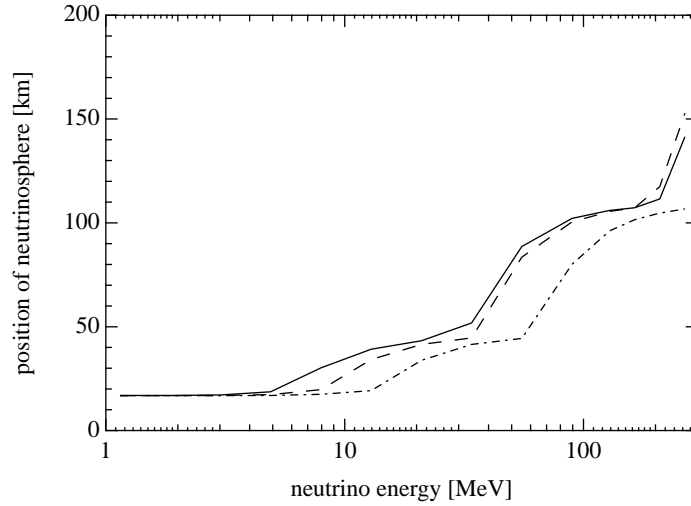


Fig. 14.— The positions of neutrinosphere for ν_e , $\bar{\nu}_e$ and $\nu_{\mu/\tau}$ are shown as a function of neutrino energy by solid, dashed and dot-dashed lines, respectively, at $t_{pb}=1$ sec for model SH.

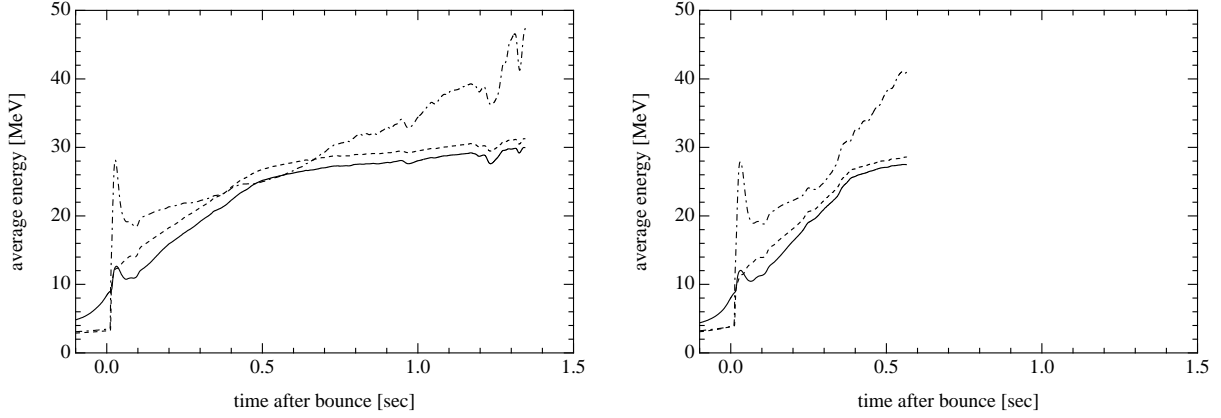


Fig. 15.— Average energies of ν_e (solid), $\bar{\nu}_e$ (dashed) and $\nu_{\mu/\tau}$ (dot-dashed) as a function of time (t_{pb}) in models SH (left) and LS (right).

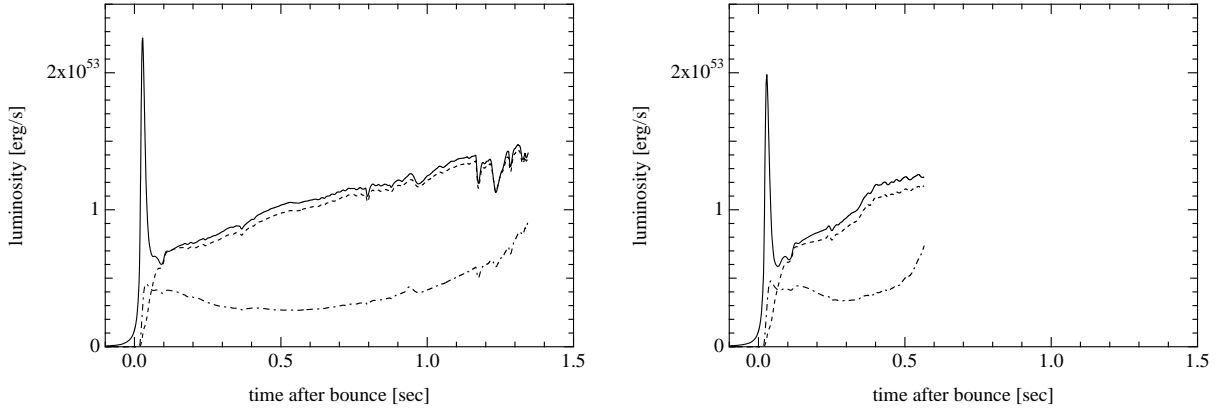


Fig. 16.— Luminosities of ν_e (solid), $\bar{\nu}_e$ (dashed) and $\nu_{\mu/\tau}$ (dot-dashed) as a function of time (t_{pb}) in models SH (left) and LS (right).

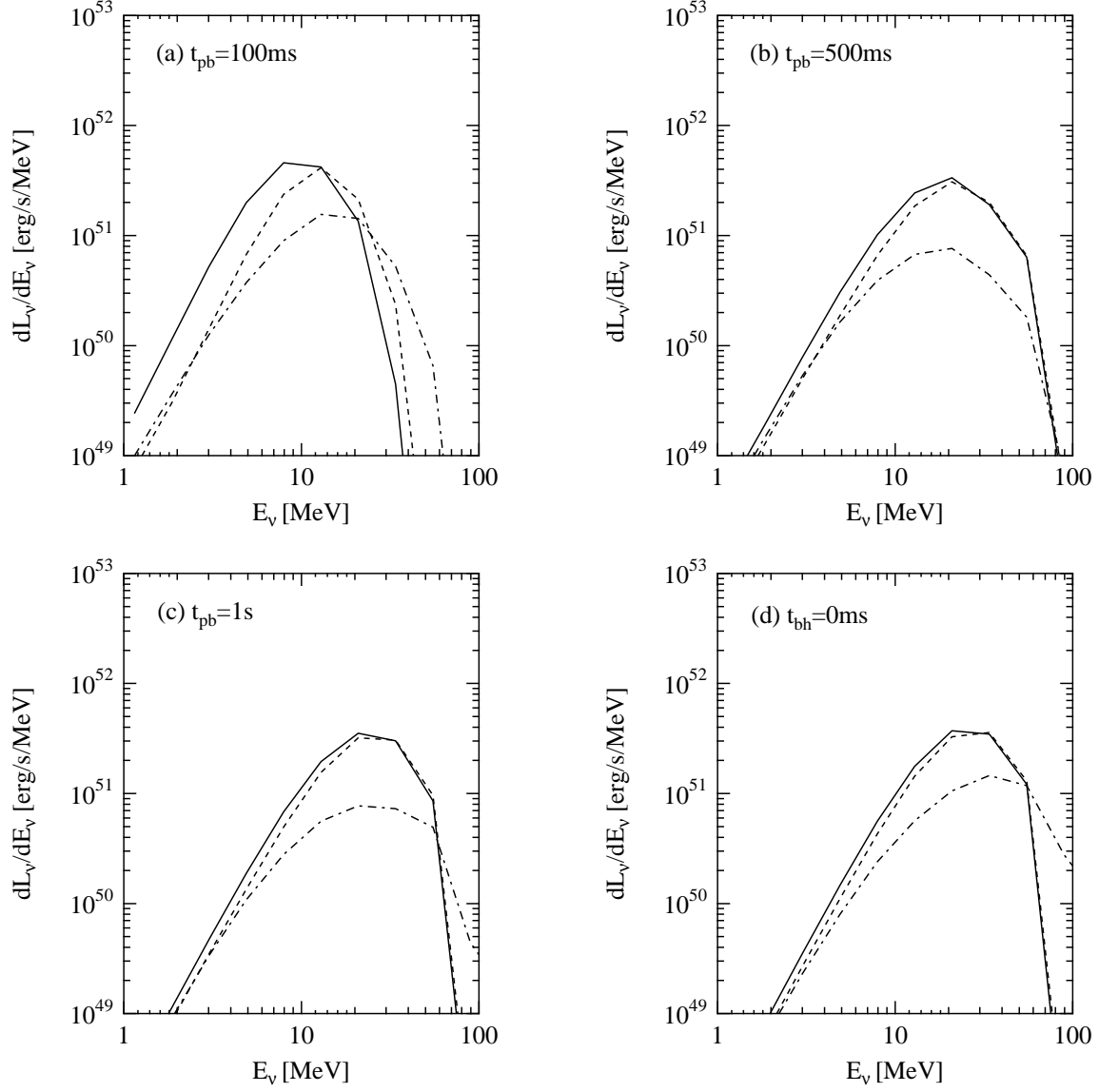


Fig. 17.— Energy spectra are shown as a function of neutrino energy for ν_e , $\bar{\nu}_e$ and $\nu_{\mu/\tau}$ by solid, dashed and dot-dashed lines, respectively, at $t_{pb}=100$ msec, 500 msec, 1 sec and $t_{bh}=0$ for model SH.

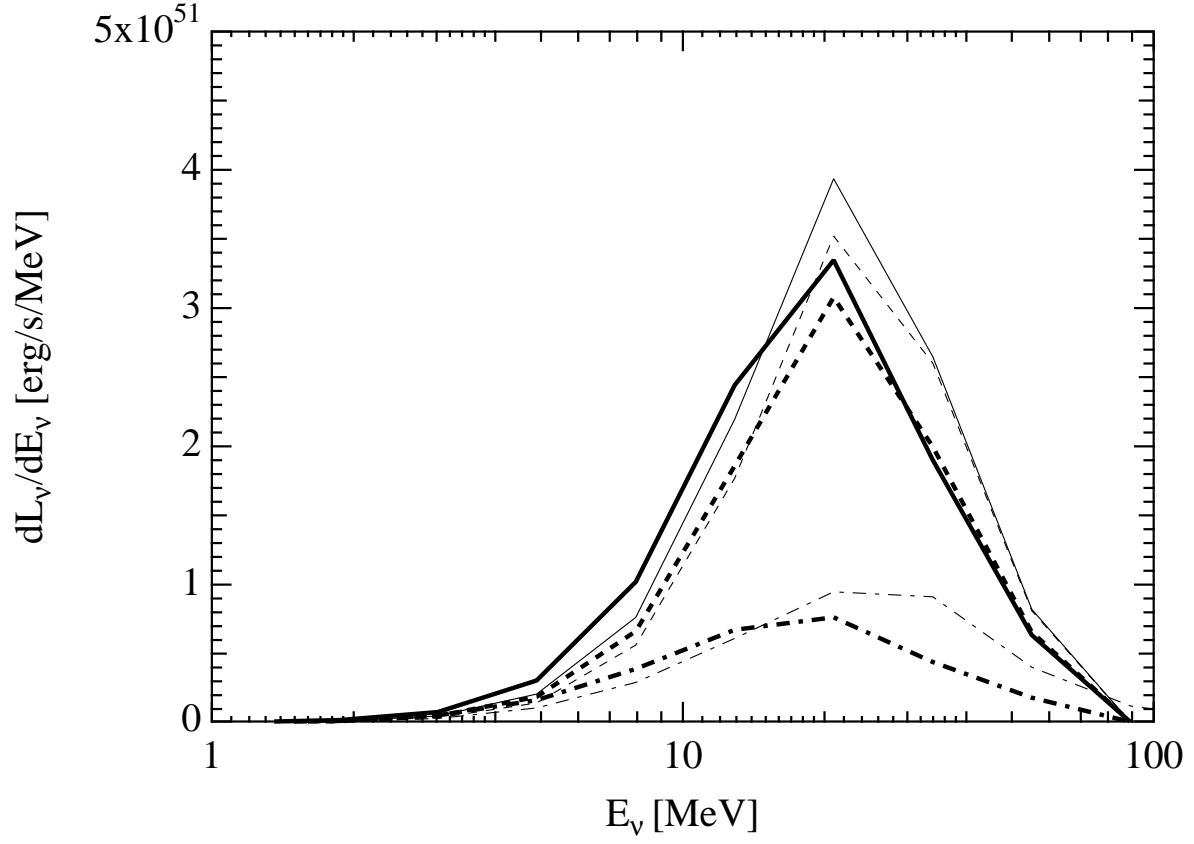


Fig. 18.— Energy spectra are shown as a function of neutrino energy for ν_e , $\bar{\nu}_e$ and $\nu_{\mu/\tau}$ by solid, dashed and dot-dashed lines, respectively, at $t_{pb}=500$ msec for model SH (thick) and LS (thin).

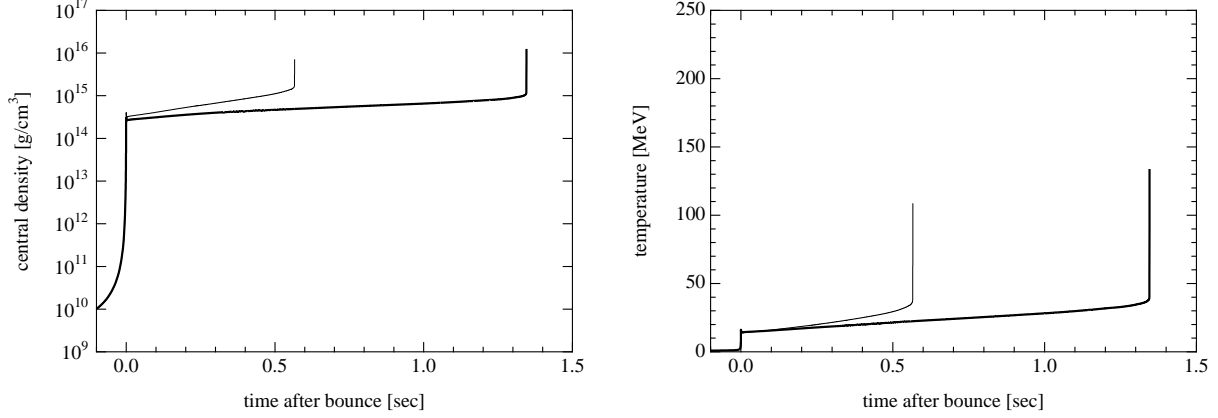


Fig. 19.— Density (left) and temperature (right) along the trajectory at center are shown as a function of time (t_{pb}) for models SH (thick) and LS (thin).

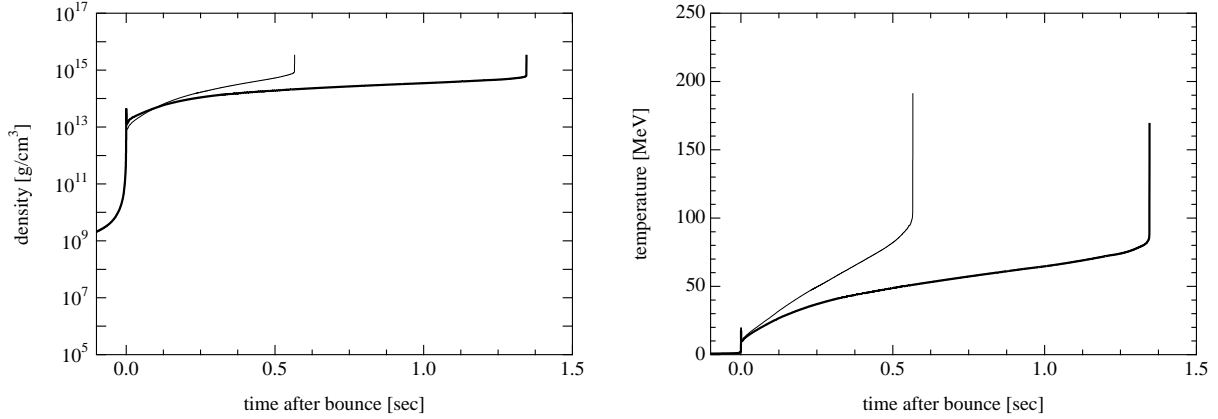


Fig. 20.— Density (left) and temperature (right) along the trajectory at $M_b=0.6M_\odot$ are shown as a function of time (t_{pb}) for models SH (thick) and LS (thin).